**Massachusetts Institute of Technology**

# Fracture clustering effect on amplitude variation with offset and azimuth analyses

Xinding Fang[1], Yingcai Zheng[2], and Michael C. Fehler[3]

## ABSTRACT

Traditional amplitude variation with offset and azimuth (AVOAz) analysis for fracture characterization extracts fracture properties through analysis of reflection AVOAz to determine anisotropic parameters (e.g., Thomsen's parameters) that are then related to fracture properties. The validity of this method relies on the basic assumption that a fractured unit can be viewed as an equivalent anisotropic medium. As a rule of thumb, this assumption is taken to be valid when the fracture spacing is less than $\lambda/10$. Under the effective medium assumption, diffractions from individual fractures destructively interfere and only specular reflections from boundaries of a fractured layer can be observed in seismic data. The effective medium theory has been widely used in fracture characterization, and its applicability has been validated through many field applications. However, through numerical simulations, we find that diffractions from fracture clusters can significantly distort the AVOAz signatures when a fracture system has irregular spacing even though the average fracture spacing is much smaller than a wavelength (e.g., $\ll \lambda/10$). Contamination by diffractions from irregularly spaced fractures on reflections can substantially bias the fracture properties estimated from AVOAz analysis and may possibly lead to incorrect estimates of fracture properties. Additionally, through Monte Carlo simulations, we find that fracture spacing uncertainty inverted from amplitude variation with offset (AVO) analysis can be up to 10%–20% when fractures are not uniformly distributed, which should be the realistic state of fractures present in the earth. Also, AVOAz and AVO analysis gives more reliable estimates of fracture properties when reflections at the top of the fractured layer are used compared with those from the bottom of the layer.

## INTRODUCTION

Naturally fractured reservoirs occur worldwide. The most important impact of fractures on oil field exploration and production is their influence on fluid flow. Natural fracture systems can dominate the fluid drainage pattern for reservoirs in rocks with low matrix permeability. Thus, knowledge about the spatial distribution and mechanical property of fracture systems is important for improved drilling and enhanced oil recovery.

Traditional seismic methods for fracture characterization retrieve fracture information by analyzing reflection P-wave amplitude variation with offset and azimuth (AVOAz) (Rüger, 1998; Shen et al., 2002; Hall and Kendall, 2003; Shaw and Sen, 2006; Liu et al., 2010; Lynn et al., 2010) or by studying S-wave splitting (Gaiser and Van Dok, 2001; Van Dok et al., 2001; Angerer et al., 2002; Crampin and Chastin, 2003; Vetri et al., 2003). Both methods view fractured reservoirs as an equivalent anisotropic medium based on the assumptions that fractures are spatially dense and that their spacing is much smaller than a seismic wavelength. Effective medium-based approaches use specularly reflected waves (P-to-P or P-to-S) for fracture characterization (Shaw and Sen, 2004). However, individual fractures can scatter seismic energy and produce scattered waves even when fracture spacing is comparable with the seismic wavelength (Willis et al., 2006; Fang et al., 2014). Willis et al. (2006), Fang et al. (2013b, 2014), and Zheng et al. (2013) develop different scattering/diffraction-based methods to extract fracture information by analyzing the characteristics of multiple scattered waves by fractures. The scattering-based methods are

---

[1]Formerly Massachusetts Institute of Technology, Department of Earth, Atmospheric, and Planetary Sciences, Cambridge, Massachusetts, USA; presently South University of Science and Technology of China, Department of Ocean Science and Engineering, Shenzhen, China. E-mail: fangxinding@gmail.com.
[2]University of Houston, Department of Earth and Atmospheric Sciences, Houston, Texas, USA. E-mail: yzheng12@uh.edu.
[3]Massachusetts Institute of Technology, Department of Earth, Atmospheric, and Planetary Sciences, Cambridge, Massachusetts, USA. E-mail: fehler@mit.edu.

more general than AVOAz approaches, and their results can be approximated by the effective medium approaches under a low-frequency assumption. However, laboratory experiments (Fang et al., 2014; Zhu et al., 2015) show that specular reflections and fracture diffractions from a fractured layer can have a similar magnitude and they may interfere with each other in seismic analysis. This leads to the speculation that scattering from individual fractures may affect AVOAz analysis when fractures are not uniformly distributed, and this calls into question the validity of the effective medium assumption.

A fracture is a structural discontinuity in a rock and usually consists of two subparallel and more-or-less planar surfaces (Pollard and Segall, 1987). The effective medium schemes of Hudson (1980) and Schoenberg (1980) are the two most popular theories for modeling seismic responses of fractures. In Hudson's theory, a natural fracture is simulated as a planar distribution of small isolated cracks. In Schoenberg's theory, a fracture is described by using a linear-slip boundary condition. The two theories predict similar elastic response of a fractured rock when the crack density is sufficiently small (Liu et al., 2000; Grechka and Kachanov, 2006). The accuracy of Hudson's theory decreases when the crack density is large, whereas Schoenberg's theory does not break down for large crack density (Grechka and Kachanov, 2006). We use Schoenberg's linear-slip theory in this study. The elastic properties of a fracture are described by the fracture compliance matrix (Schoenberg, 1980), which depends on the geometry of the fracture surface and the material that fills the fracture (Schoenberg and Sayers, 1995; Liu et al., 2000; Brown and Fang, 2012).

We simulate the influence of fractures on seismic wave propagation using the effective medium model (EMM) and the discrete fracture model (DFM) separately (Zhang et al., 2005). In the EMM, a fractured layer is treated as a homogeneous anisotropic layer whose elastic properties are calculated from the given background rock properties, fracture density, and fracture compliance (Schoenberg and Sayers, 1995). In the DFM, individual fractures are modeled using a finite-difference (FD) approach as imperfect slip interfaces embedded in the background formation (Coates and Schoenberg, 1995). We assume that fractures are vertical and parallel to each other in the simulations because subsurface natural fracture planes tend to be vertical and parallel to the maximum horizontal stress direction (Zoback, 2010). Previous numerical and experimental studies (Tadepalli et al., 1995; Fatkhan et al., 2001; Alhussain et al., 2007; Chichinina et al., 2009; Mahmoudian et al., 2012; Far et al., 2014) on models with regularly spaced fractures have demonstrated that the EMM and DFM models are equivalent when fracture spacing is sufficiently small compared with the wavelength (e.g., $< \lambda/10$), which is the foundation for the use of EMM in fracture characterization. However, fractures are unlikely to be uniformly distributed in the earth. We will investigate numerically the influence of fracture spatial distribution on AVOAz analysis through comparing results obtained from the two different models.

## LINEAR SLIP FRACTURE MODEL

When a system of parallel fractures is embedded in a homogeneous isotropic background medium, the effective stiffness matrix of the medium is given as (Schoenberg and Sayers, 1995)

$$C = \begin{bmatrix} M(1-\delta_N) & \Lambda(1-\delta_N) & \Lambda(1-\delta_N) & & & \\ \Lambda(1-\delta_N) & M(1-r^2\delta_N) & \Lambda(1-r\delta_N) & & & \\ \Lambda(1-\delta_N) & \Lambda(1-r\delta_N) & M(1-r^2\delta_N) & & & \\ & & & \mu & & \\ & & & & \mu(1-\delta_T) & \\ & & & & & \mu(1-\delta_T) \end{bmatrix},$$

(1)

with

$$M = \Lambda + 2\mu, \tag{2}$$

$$r = \frac{\Lambda}{M}, \tag{3}$$

$$\delta_N = \frac{d_f Z_N M}{1 + d_f Z_N M}, \tag{4}$$

$$\delta_T = \frac{d_f Z_T \mu}{1 + d_f Z_T \mu}, \tag{5}$$

where $\Lambda$ and $\mu$ are the Lame parameters, $Z_N$ and $Z_T$ are the normal and tangential compliances of a single fracture and all fractures are assumed to have identical elastic properties, $d_f$ is the fracture spatial density that is defined as the number of fractures per unit distance, and the fracture symmetry axis is assumed to be along the $x$-axis direction. Note that $Z_N$ and $Z_T$ in the paper of Schoenberg and Sayers (1995) are defined as the average compliances of a set of parallel fractures. However, $Z_N$ and $Z_T$ in equations 4 and 5 refer to the normal and shear compliances of an individual fracture and the product of individual fracture compliance and fracture density gives the corresponding total fracture compliance per unit volume.

In the EMM, the stiffness of a fractured unit is calculated using equation 1, in which $d_f$ is taken as the spatial density of fractures over a representative distance along the $x$-direction. In the DFM, we use the method of Coates and Schoenberg (1995) to model seismic wave scattering by the discrete fractures. The linear-slip boundary condition of individual fractures is implemented by adding a fracture-induced excess compliance, which is a function of $Z_N$ and $Z_T$, to the stiffness tensor of those grid cells intersecting the fracture planes.

## FRACTURE SPATIAL DISTRIBUTION FUNCTION

For simplicity, fracture planes are assumed to be vertical and they are parallel to each other in our numerical models. In this case, the only spatial variable is the fracture spacing, which is defined as the distance between two neighboring fractures. For natural fractures, observations in exposed outcrops showed that the distribution of fracture spacing follows a power-law function (Priest and Hudson, 1976; Bonnet et al., 2001). To generate a random fracture model with fracture spacing distribution following a power-law function, we set

$$\frac{a^n - a_{\min}^n}{a_{\max}^n - a_{\min}^n} = m, \tag{6}$$

where $a$ is the fracture spacing, $n$ is the power-law exponent governing the distribution, $m$ is a random number within the range of [0, 1], and $a_{\min}$ and $a_{\max}$ are the minimum and maximum values for fracture spacing, respectively. From equation 6, we have

$$a = [a_{\min}^n + m \cdot (a_{\max}^n - a_{\min}^n)]^{\frac{1}{n}}. \tag{7}$$

We can obtain models with different fracture spatial distributions by changing the value of $n$. Figure 1 is a schematic showing the fracture spacing distribution with different values of $n$. When $n = 1$, we get uniformly random distribution; when $n < 0$, we have power-law random distribution. In the following modeling section, we will see that random distribution can lead to the formation of clusters of fractures in the fracture systems generated from equation 7.

## NUMERICAL MODELING OF SEISMIC WAVE SCATTERING BY RANDOM FRACTURES

In numerical simulations, we use a 3D FD modeling program to simulate elastic seismic wave propagation for EMM and DFM (Fang et al., 2014). The accuracy of our numerical simulation program has been validated through comparison with the boundary element method (Chen et al., 2012). The same program was also used in the study of fracture characterization from seismic scattered waves (Fang et al., 2013b, 2014; Zheng et al., 2013). We will first present the 3D simulation results and then investigate in more detail the influence of different fracture spatial distributions on the AVO analysis through 2D Monte Carlo simulations. We use the Ricker wavelet as the seismic source wavelet.

### 3D simulations

We use equation 7 with $n = -1$ as well as $a_{\min} = 5$ m and $a_{\max} = 30$ m to generate a random fracture model whose fracture spacing follows a power-law distribution. Figure 2 shows the spatial distribution of 165 fractures in the model. The mean fracture spacing is 12 m. The fracture spacing in the model varies from 5 to 30 m in steps of 2.5 m, which is the grid size in the subsequent numerical simulations. The solid black curve gives the spacing averaged over a 150 m wide window. The histogram on the right (Figure 2) shows the statistics of the number of neighboring fractures whose spacing is within a spatial interval. We assume that all fractures are vertical and parallel to the $y$-direction and they have the same normal ($Z_N$) and tangential ($Z_T$) fracture compliances, which are set to be $10^{-10}$ m/Pa. This may represent stiff gas-filled fractures (Daley et al., 2002; Sayers et al., 2009). The P- and S-wave velocities of the background matrix are 3.0 and 1.7 km/s, respectively. The density is 2.2 g/cm$^3$. Figure 3

shows the spatial variations of the Thomsen anisotropic parameters $\varepsilon^{(V)}$, $\gamma^{(V)}$, and $\delta^{(V)}$ (Rüger, 1997) computed from the local mean fracture spacing (black curve in Figure 2) using equation 1. The model exhibits weak anisotropy because the fractures are relatively stiff. The assumption of $Z_N = Z_T$ results in $\varepsilon^{(V)} = \delta^{(V)}$, which represents elliptical anisotropy.

Figure 4 shows a 3D view of the model and the seismic data acquisition geometry. The power-law function generates a system of fractures that exhibit the spatially clustering characteristic. The model dimensions in the $x$- and $y$-directions are 2000 and 1500 m, respectively. A 150 m thick fractured layer extends from 500 to 650 m in depth. We use a thick layer to avoid tuning effects
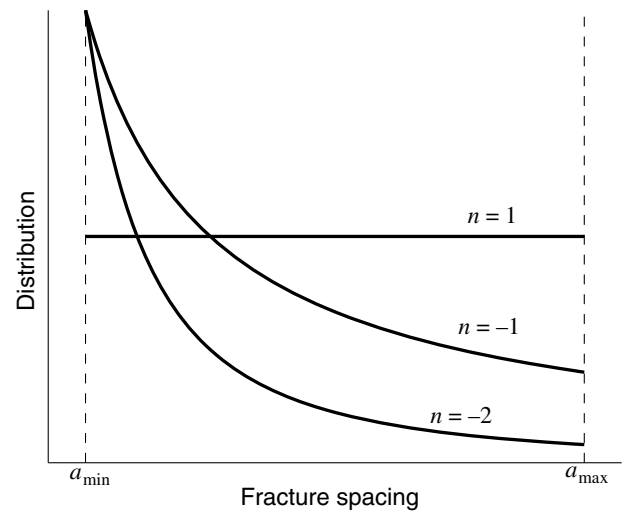


Figure 1. Fracture spacing distribution (equation 7) with different values of $n$.
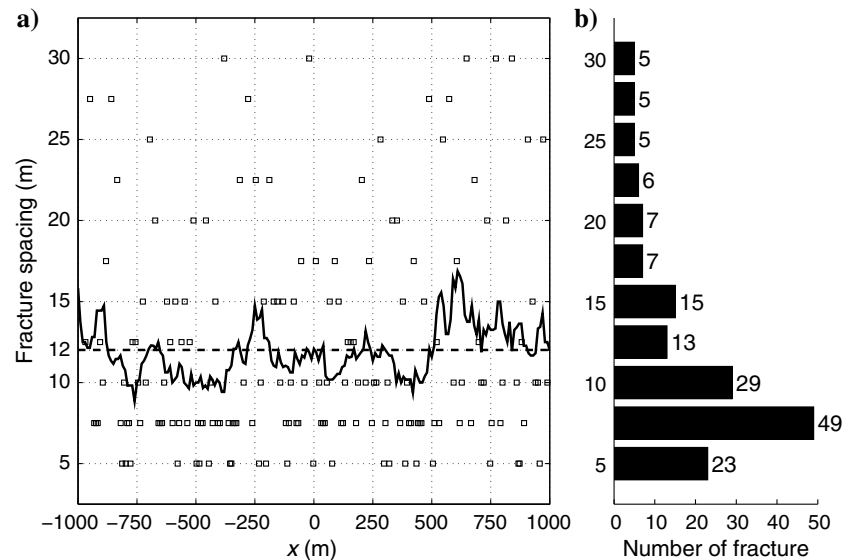


Figure 2. (a) Fracture spacing variation and (b) distribution. The squares represent the fracture spacing measured at the midpoint of every two neighboring fractures. The dashed line represents the average fracture spacing, which is 12 m. The solid curve gives the local mean fracture spacing that is averaged over a window of one P-wave wavelength, 150 m, at the dominant frequency.

caused by a thin fractured layer. In FD modeling, perfectly matched layers are added to all model boundaries to exclude boundary reflections. The gray stripes in the fractured layer represent the positions of the vertical fractures that are parallel to the y-direction. Common-midpoint (CMP) gathers are collected at 21 positions (red stars) that are located at the center of the model y-dimension and spread along the x-direction from −500 to 500 m in steps of 50 m ($x = 0$ at center). In each CMP gather, pressure data are collected at 18 azimuths from 0° to 170° at every 10° and at offsets from 300 to 600 m with a 100 m interval. In this study, we only use the pressure data although our FD modeling is elastic. The azimuthal

angle is measured counterclockwise from the positive x-direction. The strike of the fractures is at 90°.

### Uniformly distributed fractures

To investigate the validity of the EMM theory, we construct two different models with uniform fracture spacing ($a = 12$ and 20 m, respectively). For each model, we simulate seismic wavefields using two different methods, the EMM and the DFM. In the EMM, we treat the fractured layer as a homogeneous anisotropic layer (Schoenberg and Sayers, 1995), whereas in the DFM, the fractures are localized and scattering can occur among them. The two methods give the same waveforms (Figure 5). As a result, their corresponding AVAz responses (Figure 6) obtained from EMM and DFM are also the same. The AVAz amplitude is measured as the maximum absolute amplitude of the P-wave (pressure) reflection in the modeled seismic data. The exact agreement (apart from numerical precision) in the waveforms (Figure 5) and the AVAz curves (Figure 6) indicates that EMM and DFM give identical results when fractures are uniformly spaced and the seismic wavelength is much larger than fracture spacing ($\lambda/a$ is respectively 12.5 and 7.5 for these two models). This validates the accuracy of our modeling approaches and the validity of the EMM for equally spaced fracture systems.

### Randomly distributed fractures

However, it is not clear whether the EMM and the DFM will still have the same excellent agreement when fractures are randomly distributed.
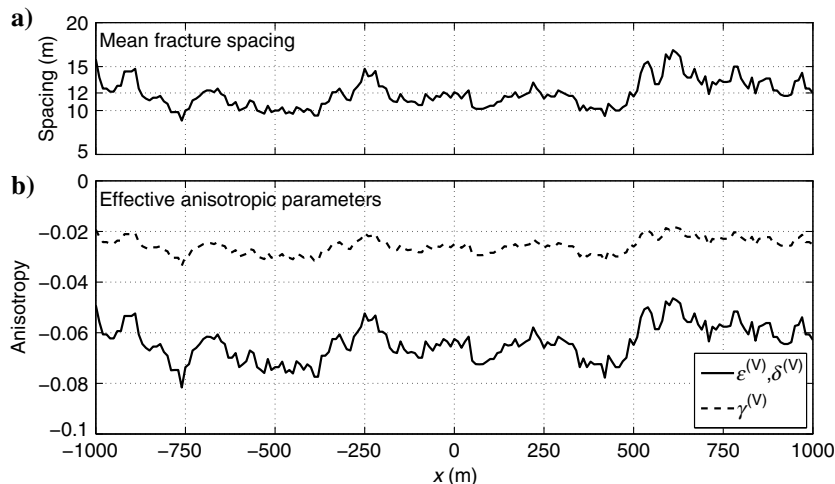


Figure 3. Effective Thomsen's anisotropic parameters $\varepsilon^{(V)}$, $\gamma^{(V)}$, and $\delta^{(V)}$, which are defined with respect to the vertical axis (Rüger, 1997), calculated using equation 1 from the local mean fracture spacing in Figure 2.
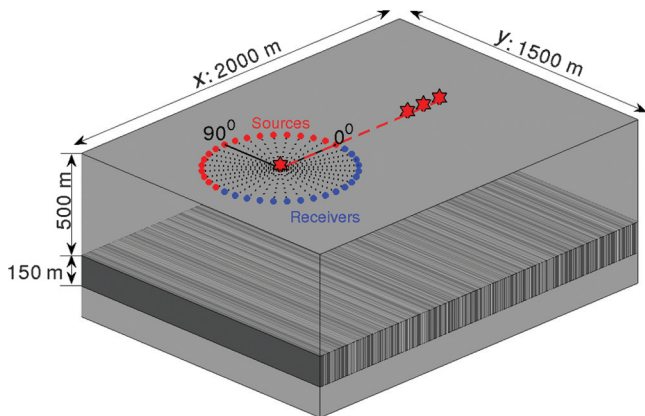


Figure 4. Three-dimensional fracture model and the acquisition geometry. The model dimensions in the x- and y-directions are 2000 and 1500 m, respectively. A 150 m thick fractured layer extends from 500 to 650 m in depth. The gray stripes in the fractured layer represent the positions of the vertical fractures that are parallel to the y-direction. The CMP gathers are collected at 21 CMP positions (red stars) that are located at the center of the model y-dimension and spread along the x-direction from −500 to 500 m in steps of 50 m. In each CMP gather, data are collected at 18 azimuths from 0° to 170° in steps of 10° and at offsets from 300 to 600 m with 100 m interval. The red and blue circles represent sources and receivers, respectively. The azimuthal angle is measured from the positive x-direction. The strike of the fractures is along 90°.
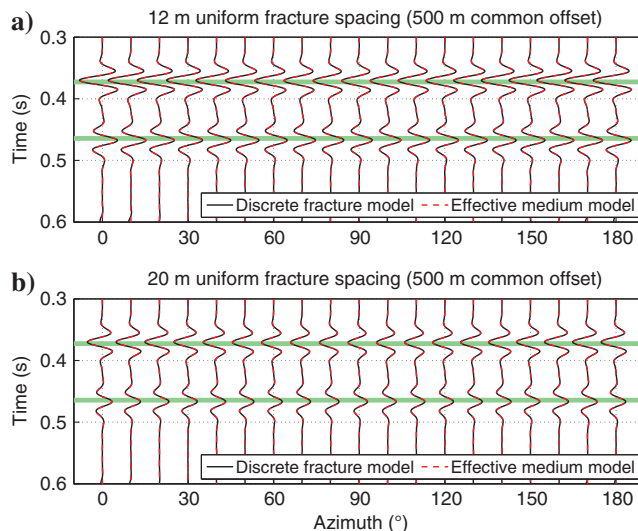


Figure 5. Comparison of the synthetic CMP gathers (pressure) obtained from DFM (black traces) and EMM (red traces) for two scenarios of 12 and 20 m uniform fracture spacing. The two green stripes in each panel indicate reflections from the top and bottom of the fractured layer. The source center frequency is 20 Hz.

Figure 7a1–7a3 shows the seismic shot gathers of the irregular fracture model (Figure 4) for source wavelets of different frequencies. We can see that the random fracture spacing has a strong influence on the wavefields even when the source frequency is set to be as low as 10 Hz ($\lambda = 300$ m $\gg$ fracture spacing). However, fracture scattering becomes very weak when the fracture system has uniform spacing, as shown in Figure 7b1–7b3, even for a 40 Hz source. This is due to the destructive interference of fracture-scattered waves. When the fracture spacing of the uniform model is increased to 20 m, the fracture-scattered waves become visible only when

$\lambda/a$ is less than 5, as shown in Figure 7c3. When fractures are irregularly spaced, fracture clusters are sensed by seismic waves as more compliant fractures whose effective spacing is much larger than the true fracture spacing. Thus, fracture clusters can turn into strong scatterers even though individual fractures are stiff. This comparison implies that fracture clustering resulting from irregularly spatial distribution of fractures can generate strong fracture scattering despite the average fracture spacing being much smaller than the seismic wavelength. This provides a strong foundation for fracture scattering (Willis et al., 2006; Zheng et al., 2013; Fang et al.,
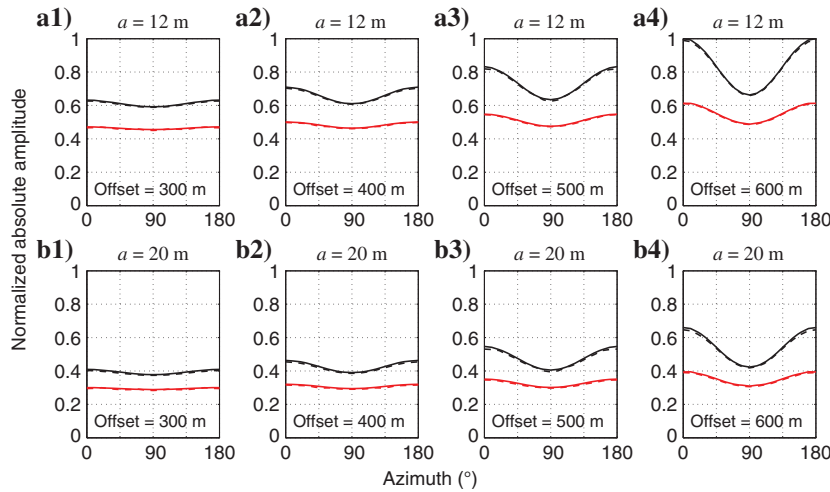


Figure 6. Comparison of the P-wave amplitude (absolute amplitude) variation with azimuth (AVAz) at four different offsets for two models that, respectively, have (a1-a4) 12 and (b1-b4) 20 m uniform fracture spacing. The waveforms at 500 m offset are shown in Figure 5. The black and red curves, respectively, show the azimuthal amplitude variation for reflections from the top and bottom of the fractured layer. The solid and dashed curves represent the data obtained from DFM and EMM, respectively. Here, $a$ denotes fracture spacing.
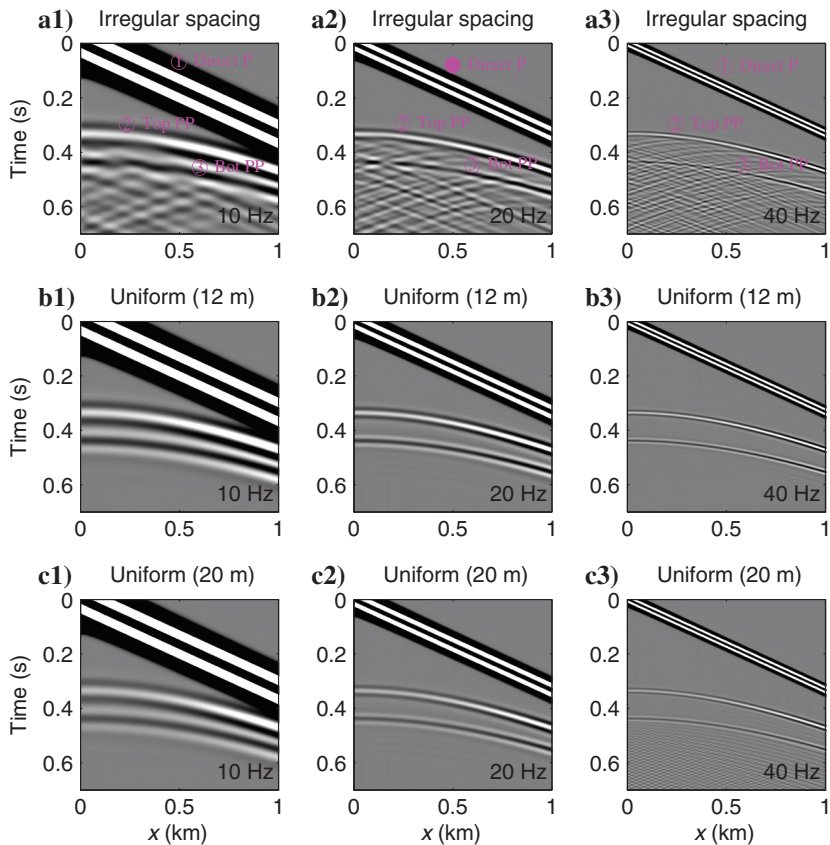


Figure 7. Synthetic shot gathers (pressure) for the irregular fracture model (Figure 4) with sources of (a1) 10, (a2) 20, and (a3) 40 Hz center frequencies for the Ricker source wavelet, respectively. Here, panels b1-b3 and c1-c3 show the same gathers but for models respectively having 12 and 20 m uniform fracture spacing. Data are recorded along the x-direction at offsets from 0 to 1 km. Seismic event 1 is the direct P-wave, events 2 and 3 are the P-to-P reflection from top and bottom of the fractured layer, respectively.

2014) to be an effective method to characterize fractured reservoirs at large spatial scales.

Figure 8 shows the common-offset (at 500 m) CMP gathers at five different midpoint positions of the model shown in Figure 4 together with the results obtained from EMM. The source wavelet center frequency is 20 Hz. The corresponding P-wave wavelength $\lambda$

is 150 m. The EMM results at each CMP position are calculated based on the values of the local effective anisotropy parameters, as shown in Figure 3. For the reservoir top reflections, DFM and EMM results have similar phase and amplitude. However, the phase and amplitude of the waveforms obtained from DFM are significantly different from the EMM results for the reservoir

Figure 8. Common-offset CMP gathers at $x = -450, -200, 0, 50,$ and 500 m for model shown in Figure 4. The black (peak) and gray (trough) traces are the DFM results. The red traces are the EMM results. The two background green stripes in each panel indicate reflections from top and bottom of the fractured layer. The source wavelet is a 20 Hz Ricker.
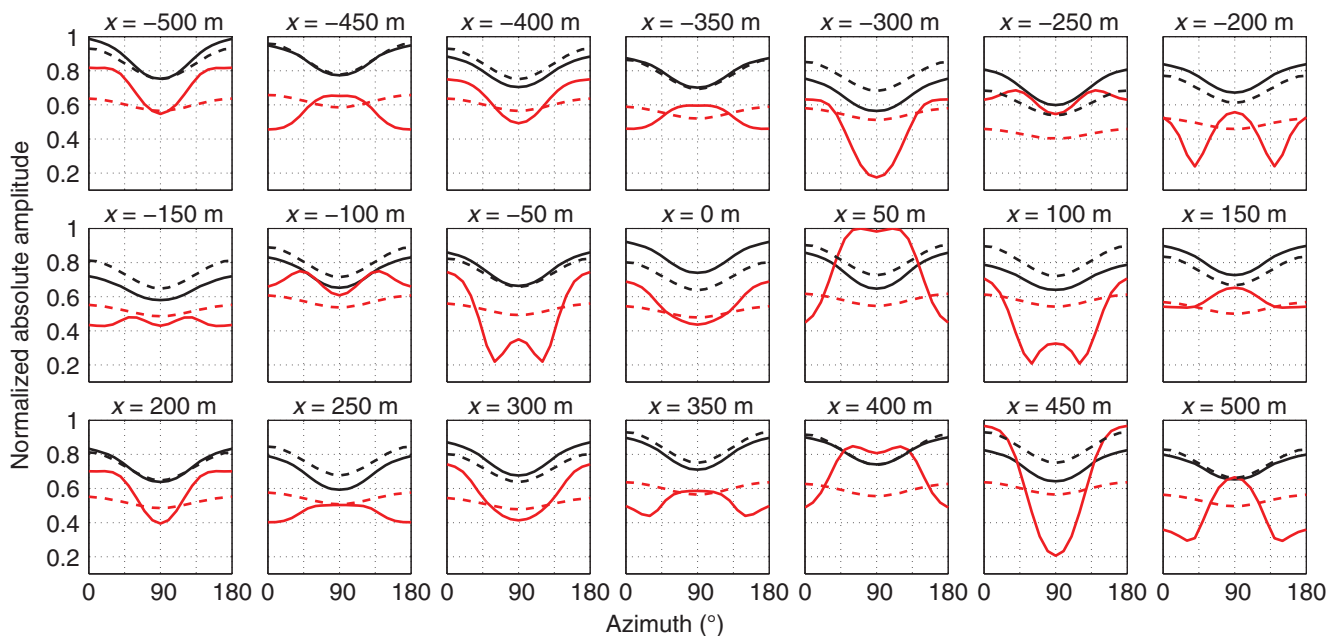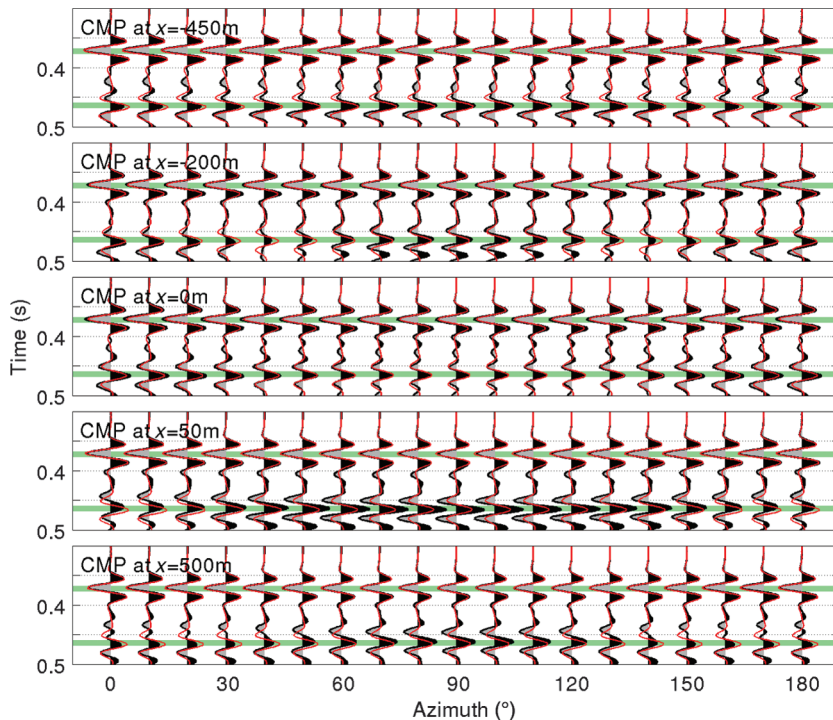


Figure 9. The AVAz responses at 500 m offset for CMP at 21 different positions. The black and red curves show the amplitude azimuthal variation for reflections from the top and bottom of the fractured layer, respectively. The solid and dashed curves represent the results obtained from DFM and EMM, respectively.

bottom reflections. Figure 9 shows the AVAz responses extracted from the 500 m common-offset CMP gathers at 21 different positions. The maximum absolute amplitude over a time window of one wavelength that centers at the predicted reflection arrival time is used for the AVAz analysis. The AVAz analyses of the top reflections obtained from DFM (solid black) follow the expected "cosine" behavior that is predicted by EMM, although the values of DFM (solid black) differ from those of EMM (dashed black) at most CMP positions. However, the AVAz analyses of the bottom reflections obtained from DFM (solid red) are strongly distorted. Figure 10 shows the Fresnel zones (Monk, 2010) for the top and bottom reflections at 500 m offset. The gray and red regions in the fractured layer represent the areas where fracture-scattered
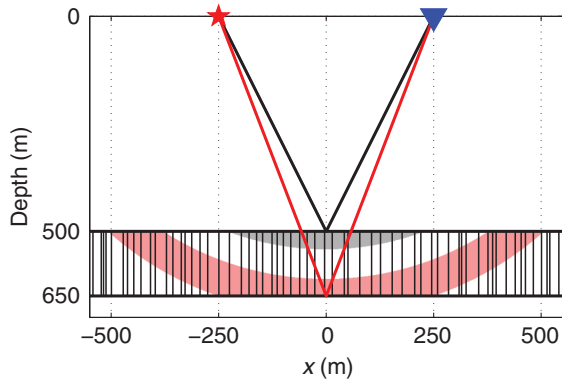


Figure 10. Highlighted gray and red regions in the fractured layer represent the first Fresnel zones, in which fracture scattered waves undergo constructive interference with the reflections from the top and bottom of the fractured layer, respectively. The black and red lines indicate the raypaths for the top and bottom reflections, respectively.

waves undergo constructive interference with the reflections from the top and bottom of the fractured layer, respectively. The Fresnel zone for the bottom reflections (red) is much wider than that for the top reflections (gray), indicating that the bottom reflections interfere with fracture-scattered waves that are generated from fractures spread over a broader region. Moreover, fracture scattering becomes stronger when it occurs further away from the midpoint because P-to-P fracture scattering generally becomes stronger when the incident angle with respect to the fracture plane increases (Fang et al., 2013a). Therefore, it is more difficult to analyze the AVAz of the bottom reflections. At short offsets, the AVAz responses show similar behavior, as shown in Figure 11. This demonstrates that the validity of the effective medium theory depends not only on the $\lambda/a$ ratio but also how the fractures are spatially distributed. In practice, if some overburden anisotropy above the fractured reservoir is present, it could introduce significant errors in fracture characterization using AVAz.

### AVAz inversion for random fractures

The DFM can accurately simulate the geometric and mechanical properties of individual fractures, whereas EMM approximates a fractured unit as a locally homogeneous anisotropic rock so that fracture properties can be inverted from the observed AVAz responses. The accuracy of the EMM-based fracture characterization methods may suffer from the effective medium assumption because natural fractures are unlikely to be uniformly distributed in the earth. To investigate the limitation of EMM in characterizing the properties of irregular fracture systems, we use EMM to invert for the fracture spacing from the AVAz responses obtained from the DFM data. To perform the inversion, we use EMM to generate a series of AVAz templates for models with uniform fracture spacing, whose value varies from 0 to 100 m with a 0.1 m interval. For the AVAz obtained from DFM at a given CMP location, we invert
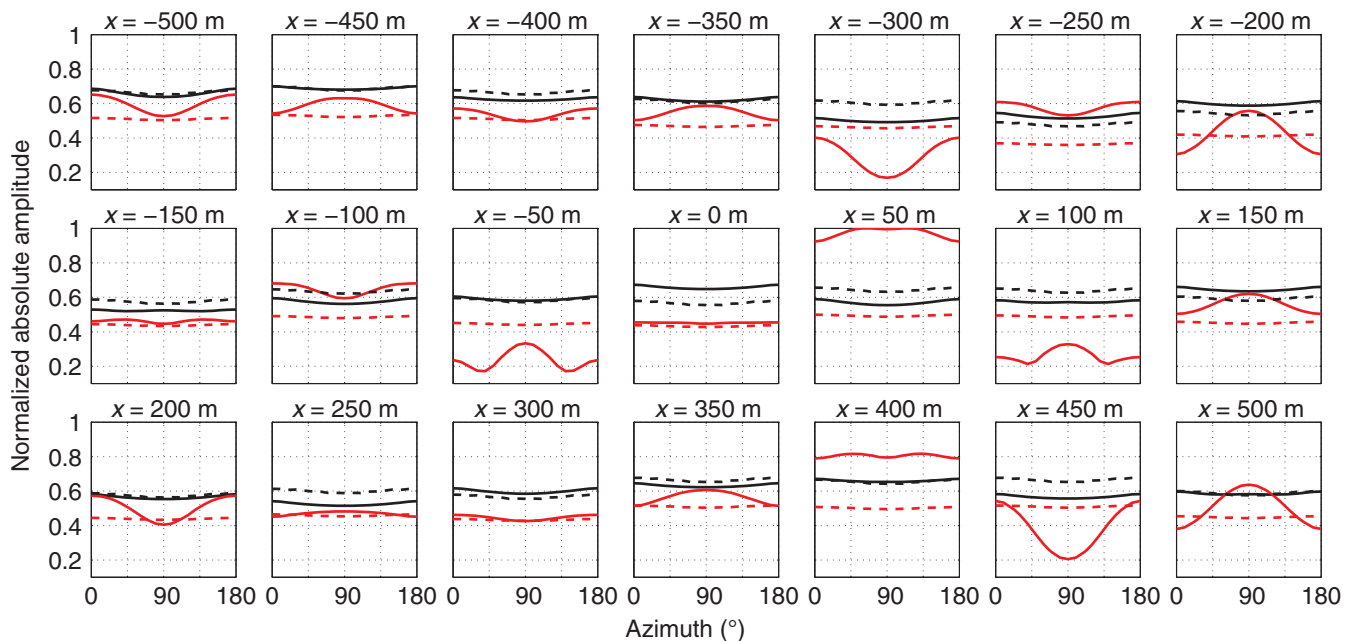


Figure 11. The same as Figure 9 except that the AVAz responses at 300 m offset are plotted.

Figure 12. Errors in the inverted fracture spacing. (a) Squares are the fracture spacing inverted from the 500 m offset AVAz responses of the top reflections. The black and gray circles respectively represent the model mean fracture spacing averaged over the ranges of $\lambda$ and $2\lambda$ at each CMP position. (b) The black and gray histograms respectively show the percentage errors of the inverted fracture spacing with respect to the mean fracture spacing in panel (a). The two dashed blue lines show the corresponding STD of the fracture spacing over the ranges of $\lambda$ (black circles) and $2\lambda$ (gray circle) at each CMP position, respectively.
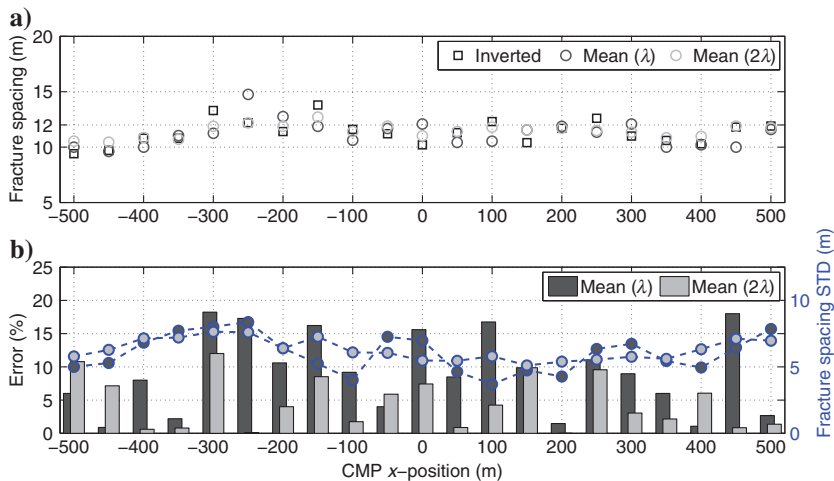
Figure 13. Errors in the inverted fracture spacing from the AVAz responses of the CMP gathers at different offsets. The black and gray histograms respectively show the errors calculated with respect to the mean spacing averaged over the regions of $\lambda$ and $2\lambda$ at each CMP position.
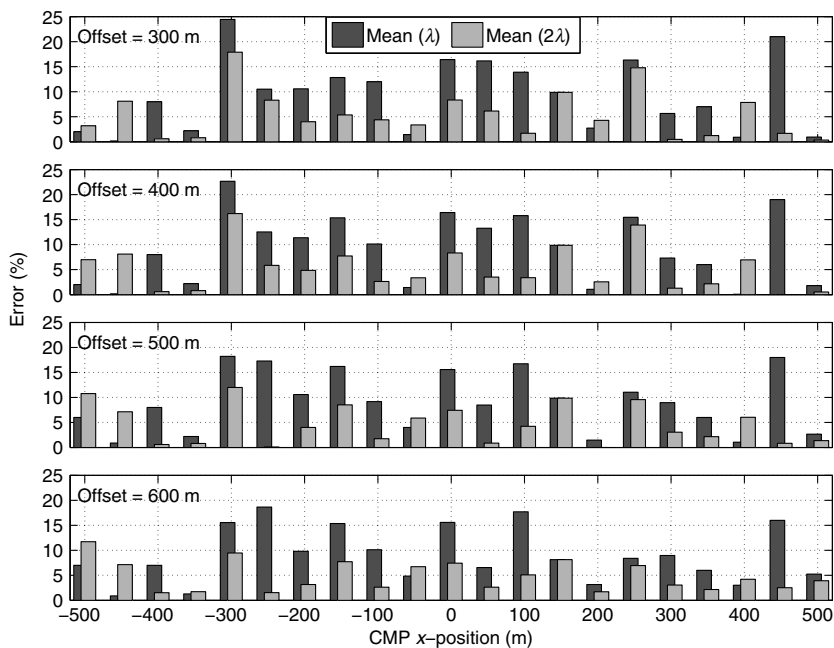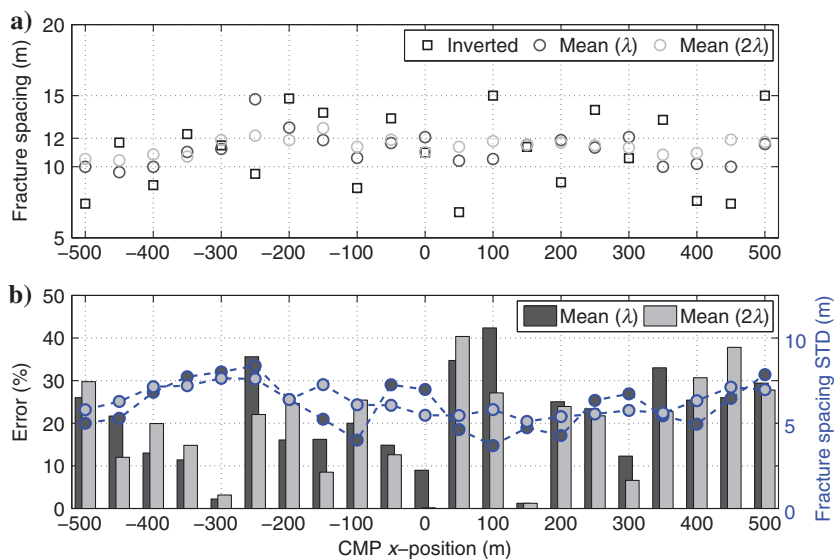
Figure 14. Same as Figure 12 except that the fracture spacing is inverted from the AVAz responses of bottom reflections.

for the local fracture spacing by searching through all the templates to find the one that minimizes the root-mean-square error with the data. Because of the trade-off between $d_f$ and the compliance $Z_N$ or $Z_T$ (equations 4 and 5), the fracture compliance is assumed to be known in the inversion.

Figure 12a shows the comparison of the fracture spacing inverted from the 500 m offset AVAz responses from the top of the fractured layer and the model mean fracture spacing averaged over the windows of $\lambda$ (150 m) and $2\lambda$ (300 m) at each CMP. Figure 12b shows the percentage errors of the inverted spacing with respect to the mean spacing averaged over the two windows together with the standard deviation (STD) of the model fracture spacing at each CMP. The inverted spacing deviates from the true mean spacing

by approximately 10%–15% for most CMPs. Variations of the errors shown in Figure 12b are not correlated with the STD (dashed blue curves) of the model fracture spacing. This implies that the difference between the inverted spacing and the true mean spacing is not simply determined by the irregularity of the distribution of fractures around each CMP. Figure 13 shows the spacing errors inverted from the AVAz responses recorded at different offsets. At each CMP, the spacing errors inverted from different offsets are similar, indicating that the AVAz responses are consistent at different offsets. Figure 14 shows the results inverted from the AVAz responses of the bottom reflections. Compared with top reflections,
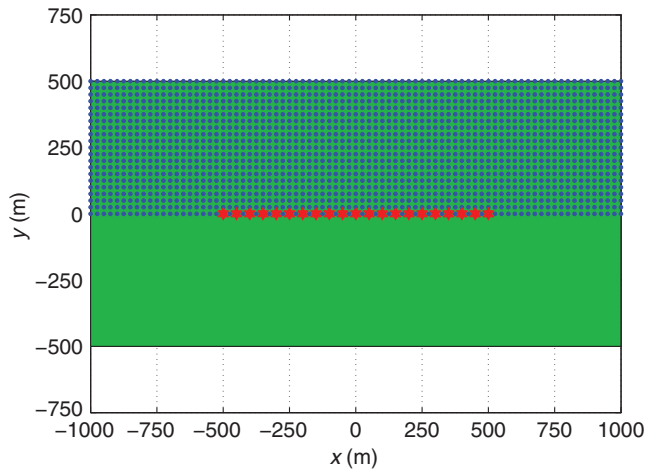


Figure 15. Seismic acquisition layout for 1701 shots. The red stars indicate the positions of 21 target CMP locations. The blue circles represent the locations of 1701 sources. The shot spacing is 25 m. Receivers with 12.5 m spacing are spread over the green area.
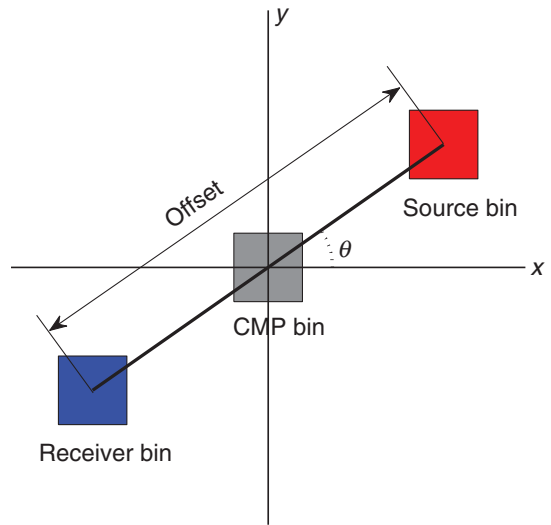


Figure 16. Schematic of azimuthal bin stacking. For a given bin size, data produced by sources within the source bin and recorded at receivers within the receiver bin and having the CMP within the CMP bin are stacked after the NMO is applied. The source, receiver, and CMP bins have the same size.
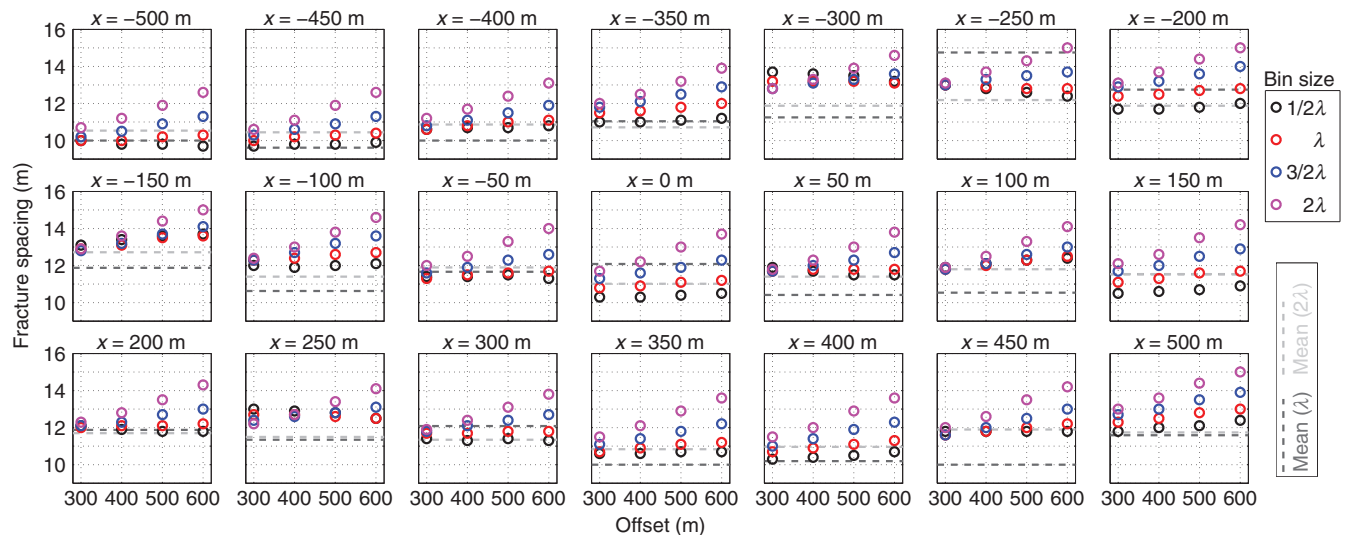


Figure 17. Fracture spacing inverted from the AVAz responses at 21 CMP positions using data stacked within bins of different sizes and at different offsets. The black, red, blue, and magenta circles respectively represent the fracture spacing inverted from data stacked within bins (see Figure 16) of $1/2\lambda$, $\lambda$, $3/2\lambda$, and $2\lambda$ width ($\lambda = 150$ m). The dashed black and gray lines in each panel respectively give the mean fracture spacing averaged over the regions of $\lambda$ and $2\lambda$ centered at the corresponding CMP. The source wavelet is a 20 Hz Ricker.

**Fang et al.**

the errors of the inverted fracture spacing from the bottom reflections are much larger, which is expected because the AVAz curves of bottom reflections are severely distorted, as shown in Figure 9. The fracture orientation is assumed to be known in fracture spacing inversion. This is a reasonable assumption for inversion using the top reflections because the AVAz curves of the top reflections follow the variation trend of the ones predicted from EMM at all CMPs (see Figure 9). However, we will obtain erroneous estimates of fracture orientation when we determine the orientation based on the characteristics of the AVAz responses of the bottom reflections. For example, the fracture orientation determined from the AVAz responses of the bottom reflections at CMPs $x = -450$, $-350$, 50, and 250 m will be 90° apart from the true orientation. It will be difficult to invert for fracture spacing or other fracture parameters if we cannot even determine the fracture orientation in the first place.

*Effect of data stacking*

It is reasonable to think that if we stack the AVAz responses using different offsets and azimuths, we might be able to reduce the effect due to random distribution of the fractures. To study the effect of data stacking on the AVAz analysis, we simulate a total of 1701 shots with 25 m shot spacing and we record the data at the model surface at every 12.5 m. The source frequency is 20 Hz. Figure 15 shows a map view of the source positions (blue circles) and the region covered by the receivers (green area). We only shot at one side of the model because the model is symmetric with respect to the $y$-axis. For each common-offset azimuthal CMP gather, we stack the data into 18 bins from 0° to 170° in steps of 10°, as illustrated in Figure 16, after normal moveout is applied. We only discuss the results for the top reflections because we find that stacking cannot help to reduce the distortion of the AVAz curves of the bottom reflections. Figure 17 shows the inverted fracture spacing from data stacked with different bin sizes at four different offsets. The estimates of fracture spacing increase with stacking bin size at most CMP positions. This variation trend is very noticeable at large

offsets, whereas it becomes less obvious at short offsets. The sensitivity of the results to the stacking bin size with offset is caused by the change of the Fresnel-zone size with incident angle and bin size (Monk, 2010). Overall, the results shown in Figure 17 suggest that stacking has little effect on mitigating the influence of fracture scattering on AVAz analysis because scattered waves generated by fracture clusters are not random and cannot be canceled.

**2D Monte Carlo simulations**

In the previous section, we investigated the fracture clustering effect on the AVAz analysis by studying the modeling results of a 3D model with irregular fracture spacing. To further analyze the relationship between the statistical characteristics of fracture spatial distribution and the associated AVO response, we compute a series of 2D Monte Carlo simulations for models with different fracture spatial distributions. Figure 18 shows the acquisition geometry for the 2D simulations. The matrix properties, fracture compliance values, as well as depth and thickness of the fractured layer are the same as the 3D model (Figure 4). Seismic CMP data are collected at offset from 300 to 600 m in steps of 100 m. We use small FD space gridding (1 m) in the 2D simulations to model small fracture spacing. The source center frequency is 20 Hz. We simulate 18 different scenarios corresponding to different fracture distributions with different fracture spacing ranges $[a_{min}, a_{max}]$ and exponent $n$ (see equation 7). For comparison, we simulate a reference model with uniform fracture spacing for each scenario. The reference fracture spacing for a given distribution function is taken as the expected value of fracture spacing, which is given as

$$a_E = \int_0^1 [a_{min}^n + m \cdot (a_{max}^n - a_{min}^n)]^{\frac{1}{n}} dm = \frac{g_{n+1}}{g_n}, \quad (8)$$

with

$$g_k = \begin{cases} (a_{max}^k - a_{min}^k)/k, & k \neq 0, \\ \ln(a_{max}) - \ln(a_{min}), & k = 0. \end{cases} \quad (9)$$

Figure 19 shows the AVO responses for 18 different scenarios with different fracture spacing ranges and exponents $n$. In each



Figure 18. Seismic acquisition geometry for 2D simulations. The CMP data are collected at offset from 300 to 600 m in the steps of 100 m.

Table 1. Expectation $a_E$ (equation 8) of fracture spacing for 18 scenarios with different fracture spatial distribution functions.

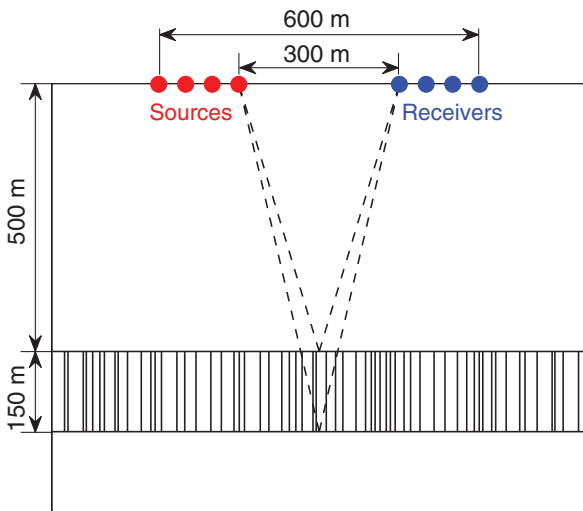| $a_{min}$ (m) | $a_{max}$ (m) | $a_E$ (m) | | |
|---|---|---|---|---|
| | | $n = 1$ | $n = -1$ | $n = -2$ |
| 2 | 4 | 3.00 | 2.77 | 2.67 |
| 2 | 8 | 5.00 | 3.70 | 3.20 |
| 2 | 12 | 7.00 | 4.30 | 3.43 |
| 5 | 10 | 7.50 | 6.93 | 6.67 |
| 5 | 20 | 12.50 | 9.24 | 8.00 |
| 5 | 30 | 17.50 | 10.75 | 8.57 |

panel, the solid black and red curves are the AVO responses of the top and bottom reflections for 100 realizations, respectively. For each scenario, the dashed black and red curves are the AVO responses of the corresponding reference model with fracture spacing $a_E$. Table 1 lists the values of $a_E$ for all scenarios studied. The AVO responses of top reflections (solid black) always follow the variation trend of the reference AVO curves (dashed black) regardless of the changes of $a_{min}$, $a_{max}$, and $n$. However, the AVO responses of bottom reflections (solid red) retain the correct variation trend only when the values of fracture spacing have a relatively narrow range (e.g., $[a_{min}, a_{max}] = [2, 4]$ and $[a_{min}, a_{max}] = [5, 10]$). When the range of fracture spacing becomes larger (e.g., $[a_{min}, a_{max}] = [5, 20]$ and $[a_{min}, a_{max}] = [5, 30]$), the AVO responses of the bottom reflections may significantly deviate from the reference ones due to large amplitude fluctuations caused by fracture cluster scattering. Overall, the top reflections have more reliable AVO responses than the bottom reflections, which is consistent with the results we obtained from the 3D modeling.

Figures 20 and 21, respectively, show the fracture spacing inverted from the AVO responses of the top and bottom reflections. Similar to the 3D study, we use a grid-search method to invert for the fracture spacing. In each panel, the horizontal and vertical axes (log scale) are, respectively, the mean fracture spacing averaged over one wavelength (i.e., 150 m) and the inverted fracture spacing. The black, red, and blue circles represent the fracture spacing found for models

with different spacing ranges, and the diagonal gray stripe represents a 10% deviation of the inverted spacing from the mean spacing. Comparing Figures 20 and 21, we can see that spacing inverted from the AVO responses of top reflections always has less deviation. However, the deviation of the inverted spacing from
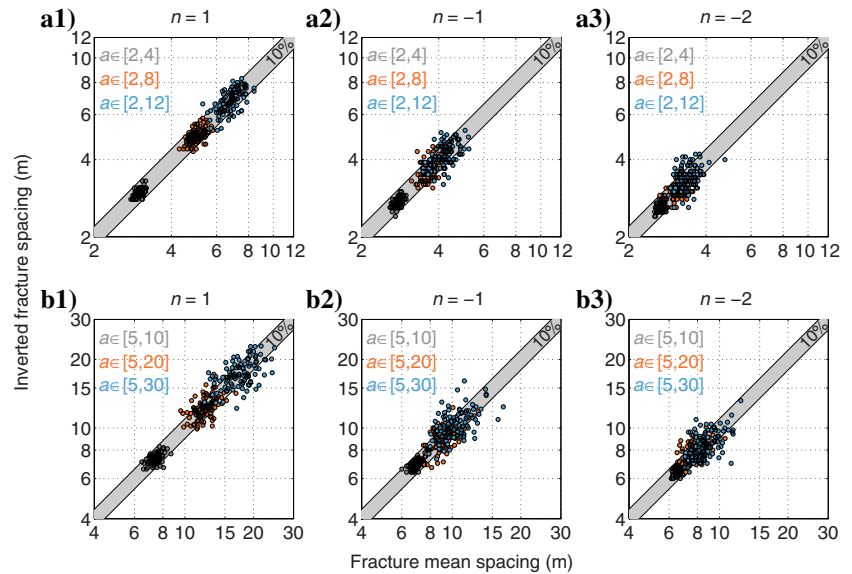


Figure 20. Inverted fracture spacing from the AVO responses of the top reflections for 18 different scenarios. The horizontal and vertical axes (log scale) are, respectively, the fracture mean spacing averaged over the region of one wavelength centered at the CMP position and the fracture spacing inverted from the AVO responses (Figure 19). The power $n$ governing the fracture spacing distribution in equation 7 is shown above each panel. The black, red, and blue circles in each panel respectively represent the results for models with different spacing ranges. The 100 realizations were generated for each case. The diagonal gray stripe represents 10% deviation of the inverted spacing from the mean spacing.
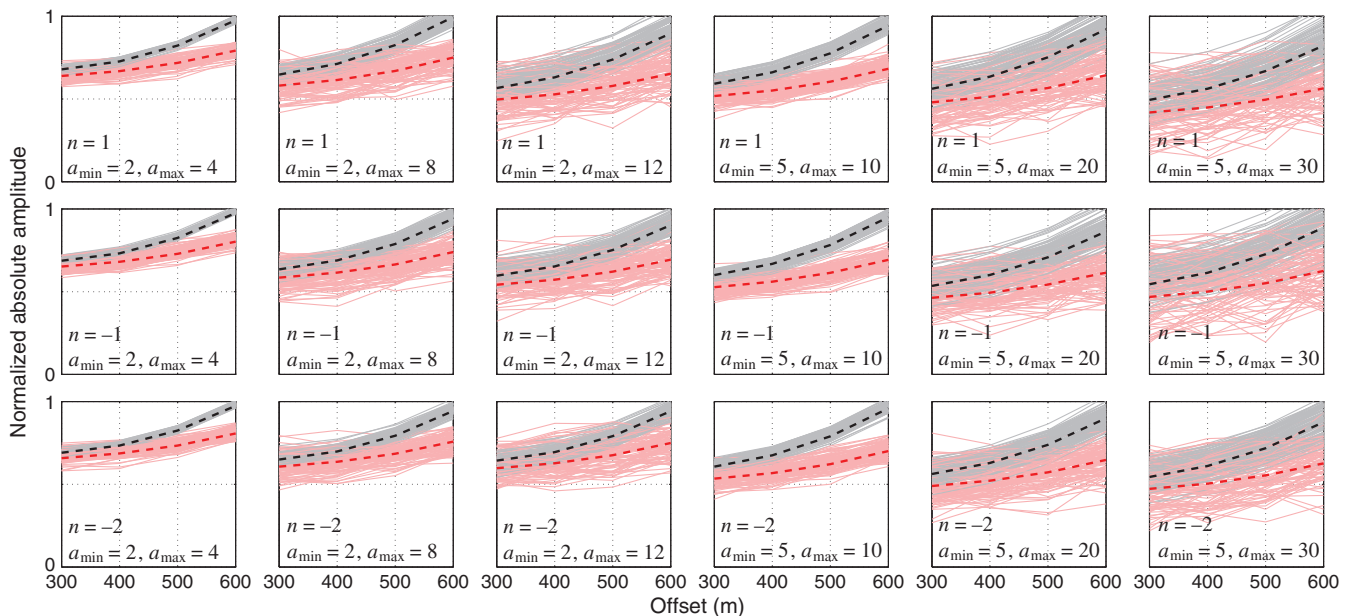


Figure 19. The P-wave AVO responses of 18 different 2D scenarios corresponding to different fracture spacing distributions (Table 1). In each panel, solid black and red curves respectively give the absolute AVO for reflections from the top and bottom of the fractured layer for 100 randomly generated models. The dashed black and red curves in each panel are the AVO responses of the corresponding reference model with uniform fracture spacing $a_E$ (equation 8).
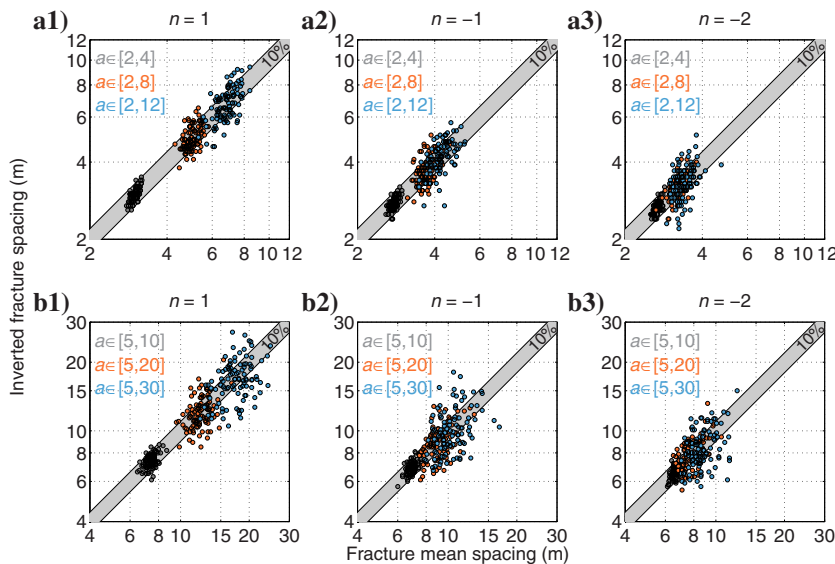
Figure 21. The same as Figure 20 except that the fracture spacing is determined from the AVO responses of the bottom reflections.

the mean spacing can still be up to 10% even for models with $[a_{min}, a_{max}] = [2, 4]$, and the deviation can increase to 20% or higher when the spacing range increases. These results suggest that EMM may not be the best model for fracture characterization because it does not account for the fracture clustering effect. Moreover, this study suggests that knowledge about the spatial distribution characteristics of fractures is vital in understanding the uncertainty of AVO results.

## CONCLUSION

Through numerical simulations, we have shown that the EMM can accurately predict the seismic responses of a fractured layer only when a fracture system has uniform fracture spacing and the spacing is less than approximately 1/5 P-wave wavelength. When fractures are irregularly spaced, clustering of fractures can develop and may be sensed by seismic waves as more compliant fractures, which generate strong scattered waves that can interfere with specular reflections from the fractured layer. The fracture clustering effects can significantly affect the characteristics of reflections from a fractured layer and cause the AVAz/AVO responses to deviate from those predicted by the effective medium theory. In our simplified numerical studies with a thick fractured reservoir, the 3D and 2D modeling results show that the fracture clustering effect can result in a more than 10% error (assuming known fracture compliance) in fracture spacing inversion even though the fracture spacing ($< \lambda/20$) is much smaller than the seismic wavelength. Therefore, the accuracy of AVAz/AVO analysis for fracture characterization may suffer from the effective medium assumption because fractures are unlikely to be uniformly distributed in the earth. To overcome this drawback, we have to consider the complete seismic response of a fracture system and take into account the fracture scattering effect in fracture characterization. It remains a future research topic to study the effect of fracture clustering for a thin fractured layer that may be a more realistic case in practice.

## REFERENCES

Alhussain, M., E. Liu, B. Gurevich, M. Urosevic, and S. Rehman, 2007, AVOAz response of a fractured medium: Laboratory measurements versus numerical simulations: 77th Annual International Meeting, SEG, Expanded Abstracts, 254–258.

Angerer, E., S. A. Horne, J. E. Gaiser, R. Walters, S. Bagala, and L. Vetri, 2002, Characterization of dipping fractures using PS mode-converted data: 72nd Annual International Meeting, SEG, Expanded Abstracts, 1010–1013.

Bonnet, E., O. Bour, N. E. Odling, P. Davy, I. Main, P. Cowie, and B. Berkowitz, 2001, Scaling of fracture systems in geological media: Reviews of Geophysics, **39**, 347–383, doi: 10.1029/1999RG000074.

Brown, S., and X. D. Fang, 2012, Fluid flow property estimation from seismic scattering data: 82nd Annual International Meeting, SEG, Expanded Abstracts, doi: 10.1190/segam2012-1315.1.

Chen, T. R., M. C. Fehler, X. D. Fang, X. F. Shang, and D. R. Burns, 2012, SH wave scattering from 2-D fractures using boundary element method with linear slip boundary condition: Geophysical Journal International, **188**, 371–380, doi: 10.1111/j.1365-246X.2011.05269.x.

Chichinina, T. I., I. R. Obolentseva, and G. Ronquillo-Jarillo, 2009, Anisotropy of seismic attenuation in fractured media: Theory and ultrasonic experiment: Transport in Porous Media, **79**, 1–14, doi: 10.1007/s11242-008-9233-9.

Coates, R. T., and M. Schoenberg, 1995, Finite-difference modeling of faults and fractures: Geophysics, **60**, 1514–1526, doi: 10.1190/1.1443884.

Crampin, S., and S. Chastin, 2003, A review of shear wave splitting in the crack-critical crust: Geophysical Journal International, **155**, 221–240, doi: 10.1046/j.1365-246X.2003.02037.x.

Daley, T. M., K. T. Nihei, L. R. Myer, E. L. Majer, J. H. Queen, M. Fortuna, J. Murphy, and R. T. Coates, 2002, Numerical modeling of scattering from discrete fracture zones in a San Juan Basin gas reservoir: 72nd Annual International Meeting, SEG, Expanded Abstracts, 109–112.

Fang, X. D., M. C. Fehler, T. R. Chen, D. R. Burns, and Z. Y. Zhu, 2013a, Sensitivity analysis of fracture scattering: Geophysics, **78**, no. 1, T1–T10, doi: 10.1190/geo2011-0521.1.

Fang, X. D., M. C. Fehler, Z. Y. Zhu, Y. C. Zheng, and D. R. Burns, 2014, Reservoir fracture characterization from seismic scattered waves: Geophysical Journal International, **196**, 481–492, doi: 10.1093/gji/ggt381.

Fang, X. D., X. F. Shang, and M. C. Fehler, 2013b, Sensitivity of time-lapse seismic data to fracture compliance in hydraulic fracturing: Geophysical Journal International, **195**, 1843–1861, doi: 10.1093/gji/ggt340.

Far, M. E., J. Figueiredo, R. Stewart, J. Castagna, D. Han, and N. Dyaur, 2014, Measurements of seismic anisotropy and fracture compliances in synthetic fractured media: Geophysical Journal International, **197**, 1845–1857, doi: 10.1093/gji/ggu101.

Fatkhan, M., Urosevic, and J. A. McDonald, 2001, Numerical and physical modeling of P-wave AVO response for fractured media: Exploration Geophysics, **32**, 279–283, doi: 10.1071/EG01279.

Gaiser, J., and R. Van Dok, 2001, Green River basin 3-D/3-C case study for fracture characterization: Analysis of PS-wave birefringence: 71st Annual International Meeting, SEG, Expanded Abstracts, 764–767.

Grechka, V., and M. Kachanov, 2006, Effective elasticity of fractured rocks: A snapshot of the work in progress: Geophysics, **71**, no. 6, W45–W58, doi: 10.1190/1.2360212.

Hall, S. A., and J. M. Kendall, 2003, Fracture characterization at Valhall: Application of P-wave amplitude variation with offset and azimuth (AVOA) analysis to a 3D ocean-bottom data set: Geophysics, **68**, 1150–1160, doi: 10.1190/1.1598107.

Hudson, J. A., 1980, Overall properties of a cracked solid: Mathematical Proceedings of the Cambridge Philosophical Society, **88**, 371–384, doi: 10.1017/S0305004100057674.

Liu, E., J. A. Hudson, and T. Pointer, 2000, Equivalent medium representation of fractured rock: Journal of Geophysical Research, **105**, 2981–3000, doi: 10.1029/1999JB900306.

Liu, E., G. Zelewski, C. P. Lu, J. Reilly, and Z. J. Shevchek, 2010, Seismic fracture prediction using azimuthal AVO analysis in a Middle East carbonate field: Workflow and mitigation of overburden effects: 70th Annual International Meeting, SEG, Expanded Abstracts, 268–272.

Lynn, H., S. R. Narhari, S. Al-Ashwak, V. K. Kidambi, B. Al-Qadeeri, and O. Al-Khaled, 2010, PP azimuthal amplitudes and acoustic impedance for fractured carbonate reservoir characterization: 70th Annual International Meeting, SEG, Expanded Abstracts, 258–262.

Mahmoudian, F., J. Wong, and G. F. Margrave, 2012, Azimuthal AVO over a simulated fractured medium: A physical modeling experiment: 82nd Annual International Meeting, SEG, Expanded Abstracts, doi: 10.1190/segam2012-0914.1.

Monk, D. J., 2010, Fresnel-zone binning: Fresnel-zone shape with offset and velocity function: Geophysics, **75**, no. 1, T9–T14, doi: 10.1190/1.3294576.

Pollard, D., and P. Segall, 1987, Theoretical displacements and stresses near fractures in rock: With applications to faults, joints, veins, dikes, and solution surfaces, *in* B. K. Atkinson, ed., Fracture mechanics of rock: Academic Press, 277–349.

Priest, S. D., and J. A. Hudson, 1976, Discontinuity spacing in rock: International Journal of Rock Mechanics and Mining Science & Geomechanics Abstracts, **13**, 135–148, doi: 10.1016/0148-9062(76)90818-4.

Rüger, A., 1997, P-wave reflection coefficients for transversely isotropic models with vertical and horizontal axis of symmetry: Geophysics, **62**, 713–722, doi: 10.1190/1.1444181.

Rüger, A., 1998, Variation of P-wave reflectivity with offset and azimuth in anisotropic media: Geophysics, **63**, 935–947, doi: 10.1190/1.1444405.

Sayers, C. M., A. D. Taleghani, and J. Adachi, 2009, The effect of mineralization on the ratio of normal to tangential compliance of fractures: Geophysical Prospecting, **57**, 439–446, doi: 10.1111/j.1365-2478.2008.00746.x.

Schoenberg, M., 1980, Elastic wave behavior across linear slip interfaces: The Journal of the Acoustical Society of America, **68**, 1516–1521, doi: 10.1121/1.385077.

Schoenberg, M., and C. M. Sayers, 1995, Seismic anisotropy of fractured rock: Geophysics, **60**, 204–211, doi: 10.1190/1.1443748.

Shaw, R. K., and M. K. Sen, 2004, Born integral, stationary phase and linearized reflection coefficients in weak anisotropic media: Geophysical Journal International, **158**, 225–238, doi: 10.1111/j.1365-246X.2004.02283.x.

Shaw, R. K., and M. K. Sen, 2006, Use of AVOA data to estimate fluid indicator in a vertically fractured medium: Geophysics, **71**, no. 3, C15–C24, doi: 10.1190/1.2194896.

Shen, F., J. Sierra, D. R. Burns, and M. N. Toksöz, 2002, Azimuthal offset-dependent attributes applied to fracture detection in a carbonate reservoir: Geophysics, **67**, 355–364, doi: 10.1190/1.1468596.

Tadepalli, S. V., J. A. McDonald, K. K. Sekharan, and R. H. Tatham, 1995, 3D AVO physical modeling experiment over a simulated fracture medium: 65th Annual International Meeting, SEG, Expanded Abstracts, 592–595.

Van Dok, R., J. Gaiser, and J. Markert, 2001, Green River basin 3-D/3-C case study for fracture characterization: Common-azimuth processing of PS-wave data: 61st Annual International Meeting, SEG, Expanded Abstracts, 768–771.

Vetri, L., E. Loinger, J. Gaiser, A. Grandi, and H. Lynn, 2003, 3D/4C Emilio: Azimuth processing and anisotropy analysis in a fractured carbonate reservoir: The Leading Edge, **22**, 675–679, doi: 10.1190/1.1599695.

Willis, M. E., D. R. Burns, R. Rao, B. Minsley, M. N. Toksöz, and L. Vetri, 2006, Spatial orientation and distribution of reservoir fractures from scattered seismic energy: Geophysics, **71**, no. 5, O43–O51, doi: 10.1190/1.2235977.

Zhang, Y., S. Chi, M. E. Willis, D. R. Burns, and M. N. Toksöz, 2005, Comparison of discrete fracture and effective media representation of fractures on azimuthal AVO: 65th Annual International Meeting, SEG, Expanded Abstracts, 305–307.

Zheng, Y., X. Fang, M. C. Fehler, and D. R. Burns, 2013, Seismic characterization of fractured reservoirs by focusing Gaussian beams: Geophysics, **78**, no. 4, A23–A28, doi: 10.1190/geo2012-0512.1.

Zhu, Z. Y., D. R. Burns, and M. C. Fehler, 2015, Laboratory experimental studies of seismic scattering from fractures: Geophysical Journal International, **201**, 291–303, doi: 10.1093/gji/ggu399.

Zoback, M. D., 2010, Reservoir geomechanics: Cambridge University Press.